




Article

Investigation on Electrical and Thermal Performance of Glass Fiber Reinforced Epoxy–MgO Nanocomposites

Janjanam Naveen ¹, Myneni Sukesh Babu ¹, Ramanujam Sarathi ^{1,*}, Ramachandran Velmurugan ², Michael G. Danikas ³ and Athanasios Karlis ³

¹ Department of Electrical Engineering, Indian Institute of Technology Madras, Chennai 600036, India; ee18d038@smail.iitm.ac.in (J.N.); ee18d003@smail.iitm.ac.in (M.S.B.)

² Department of Aerospace Engineering, Indian Institute of Technology Madras, Chennai 600036, India; ramanv@iitm.ac.in

³ Department of Electrical and Computer Engineering, Democritus University of Thrace, 67100 Xanthi, Greece; mdanikas@ee.duth.gr (M.G.D.); akarlis@ee.duth.gr (A.K.)

* Correspondence: rsarathi@iitm.ac.in

Abstract: Epoxy nanocomposites reinforced with glass fiber, have been prepared with various weight percentages (1, 3, and 5 wt.%) of MgO nanofillers to improve their electrical and thermal performance. An increase in MgO nanofiller content up to 3 wt.% tends to enhance surface discharge and corona inception voltages measured using fluorescence and UHF methods, under both AC and DC voltage profiles. Reduced initial surface potential along with increased decay rate is observed after inclusion of MgO nanoparticles. Before and after the polarity reversal phenomena, heterocharge formation is observed in the bulk of test specimens. In comparison with other test samples, the 3 wt.% sample had reflected lower electric field enhancement factor. After MgO filler was added to glass fiber reinforced polymer (GFRP) composites, the coefficient of thermal expansion (CTE) has reduced, with the 3 wt.% specimen having the lowest CTE value. TGA measurements revealed an improvement in thermal stability of the GFRP nanocomposites up on the inclusion of MgO nanofillers. Overall, the GFRP nanocomposite sample filled with 3 wt.% nano-MgO outperformed the other test samples in terms of electrical and thermal performance.

Keywords: epoxy nanocomposites; MgO; GFRP; CIV; polarity reversal; TGA; FTIR



Citation: Naveen, J.; Sukesh Babu, M.; Sarathi, R.; Velmurugan, R.; Danikas, M.G.; Karlis, A. Investigation on Electrical and Thermal Performance of Glass Fiber Reinforced Epoxy–MgO Nanocomposites. *Energies* **2021**, *14*, 8005. <https://doi.org/10.3390/en14238005>

Academic Editor: Dimitrios Kalderis

Received: 1 November 2021

Accepted: 22 November 2021

Published: 30 November 2021

Publisher's Note: MDPI stays neutral with regard to jurisdictional claims in published maps and institutional affiliations.



Copyright: © 2021 by the authors. Licensee MDPI, Basel, Switzerland. This article is an open access article distributed under the terms and conditions of the Creative Commons Attribution (CC BY) license (<https://creativecommons.org/licenses/by/4.0/>).

1. Introduction

Epoxy resin is widely utilized and has been considered to be a critical component in achieving safe operation of electrical machines [1–5]. Researchers from all around the world are working to improve the epoxy insulation performance by developing novel insulating materials by incorporating nanofillers into the base epoxy material [6–8]. Nanocomposites are considered to have a potential to revolutionize the insulation structure design of rotating machines as well as high voltage apparatus. Hildinger et al. have stated that the incorporation of SiO₂ nanofillers in epoxy-mica insulation have resulted in a highly efficient stator winding insulation, which has improved specific power output without reduction on insulation lifetime [9]. Due to their high dielectric constant, excellent stiffness, superior mechanical strength, and high corrosion resistance, glass fiber reinforced polymer nanocomposites are considered as promising insulating materials in power apparatus, along with automotive, aerospace, wind energy harvesting, and marine applications [10–12]. The addition of MgO nanofillers into the epoxy matrix has been well-recognized to increase dielectric properties and inhibit space charge accumulation [13–15]. MgO nanoparticles tend to offer superior electrical insulation qualities than other oxide fillers due to their wide energy band and high volume resistivity [16]. In addition, Andritsch et al. stated that the epoxy–MgO nanocomposites displayed less space charge buildup than pure epoxy specimens [17]. Given these considerations, MgO nanofillers were chosen for use in the

current investigation along with GFRP nanocomposites, particularly as a space charge inhibitory material.

Partial discharges (PD) in electrical machines include slot discharges, internal discharges, and end-winding discharges, which arise as a result of poor manufacturing design and a lack of maintenance [3]. According to Nitta et al., the surface discharge phenomenon tends to decrease the spark-over voltage of GFRP sample [18]. This has also been certified in recent research [19]. For safe operation of power equipment, a reliable detection of corona inception voltage (CIV) is essential. The use of an ultra-high frequency (UHF) electromagnetic (EM) sensor to detect PD has long been recognized as a sensitive method [20]. PD detection by collecting UV/blue light emission with fluorescent fibers has recently attracted widespread interest for detecting PD because of non-interference with EM signals [21,22]. The fluorescent fibers detect low-intensity emission induced by PD pulses formed during corona inception more efficiently than the standard optical fiber because of its greater capture cross-section [23].

Polymeric materials tend to build-up charge in the bulk, under the influence of strong electric fields [24]. The accumulating charge in the bulk will increase the local electric field, leading the qualities of material to degrade sooner than expected. To accomplish bi-directional power flow in an HVDC transmission system, voltage polarity reversal is necessary. During this reversal, accumulated space charge may pose a major threat to the insulator's life [25]. Surface potential decay measurement is a valuable technique for understanding numerous physical phenomena in polymers, like surface conduction and charge trapping phenomena [26]. Thus, the space charge and surface potential details of GFRP nanocomposite samples must be investigated. The use of nanomaterials in the synthesis of fiber reinforced composites has been shown to improve mechanical and thermal performance, along with their electrical characteristics [27]. The interface between matrix, filler, and glass fiber influences the composite material's thermal characteristics in general. As a result, the current research focuses on improving the electrical and thermal behavior of GFRP nanocomposites by using MgO nanoparticles.

By considering the aspects above, the following methodical experimental experiments were performed to investigate the influence of MgO nanoparticles on glass fiber reinforced epoxy material: (i) Surface discharge and corona inception studies; (ii) Surface potential and trap characteristics under switching impulse (SI) voltages; (iii) Space charge analysis under voltage polarity reversal phenomenon; (iv) Thermo gravimetric analysis; and (v) Determination of the thermal expansion coefficient.

2. Specimen Preparation and Experimental Methods

2.1. Sample Preparation Procedure

Figure 1 shows the simplified diagram for the preparation of epoxy MgO nanocomposites reinforced with glass fiber, using a vacuum assisted resin transfer mold. MgO nanofillers with a mean particle size of 20 nm have been acquired from Nanostructured & Amorphous Materials, Inc., Houston, TX, USA and was used as the filler in the nanocomposite preparation. The dried MgO nanofillers were dissolved in ethanol for an hour before being transferred to an ultrasonic bath. The nanoparticle solution was then mixed with Hatsun's Araldite CY 230-1 epoxy resin and ultra-sonicated for an hour to ensure that the nanoparticles were evenly distributed throughout the epoxy. The nanoparticle epoxy solution was shear mixed for eight hours after ultra-sonication to achieve homogeneous dispersion of nanoparticles inside the epoxy. The resultant mixture was weighed again to see if the ethanol had evaporated; if it had not, the mixture was heated in an oven such that all the ethanol had evaporated. The nanocomposite epoxy mixture was then ultra-sonicated for a further hour. Lastly, the nanocomposite epoxy mixture was blended in a 100:11 ratio with hardener (Aradur HY 951, Hatsun) and shear mixed for 3 min.

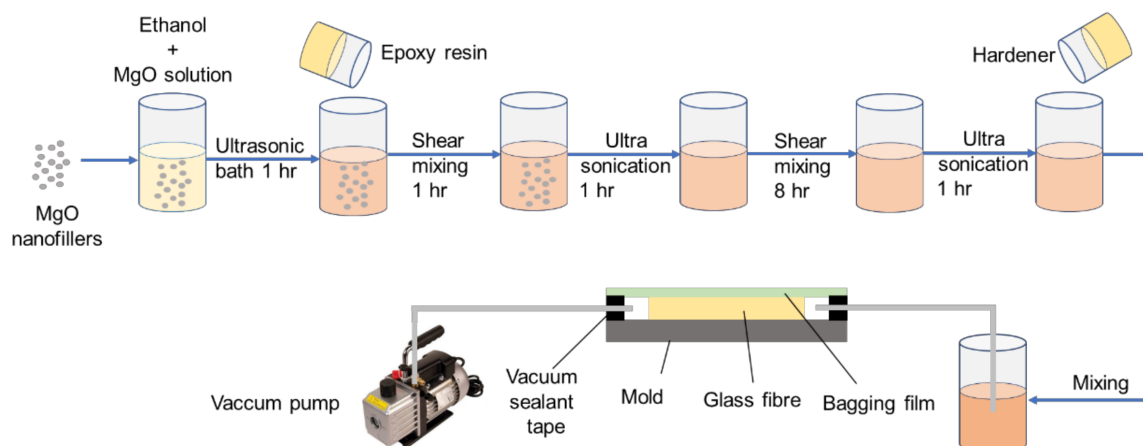


Figure 1. Schematic diagram of sample preparation.

On the glass mold, a unidirectional single layer glass fiber with thickness of 0.24 mm was kept. Vacuum bagging film and sealant tape were used to vacuum seal all four of the sides. Above the glass fiber, 2 hose pipes were introduced, one for epoxy intake and another for the vacuum inlet. The vacuum was then applied while the inlet line was closed for sucking the air out of the mold. The completed epoxy-hardener combination was then kept at intake hose, which was later opened. While the vacuum pump was on, the epoxy mixture was drawn throughout the glass fibers from the remaining hose. When the glass fiber is entirely reinforced with the epoxy mixture, both the valves are closed and left for curing at the room temperature for 24 h. After that, the GFRP–MgO nanocomposite samples were removed from the mold, washed with ethanol, and dried for four hours before being utilized in the experiment. In this work, four distinct specimens were used: one pure epoxy specimen reinforced with glass fiber and the remaining are 1, 3, and 5 wt.% MgO nano filled GFRP, represented as the 0, 1, 3, and 5 wt.%, respectively.

Earlier studies by Naveen et al., have carried out SEM analysis with GFRP epoxy nanocomposites. The results of the studies have clearly indicated that uniform dispersion of MgO in epoxy resin could be achieved up to 3 wt.% [28]. However, when the filler content was increased to 5%, non-uniform submicron agglomerations occurred, which could potentially have a poor impact with the interlinking of the nanoparticles with the polymer matrix and the glass fiber.

2.2. Corona and Surface Discharge Inception Studies

Corona along with surface discharge inception have been detected with the experimental setup depicted in Figure 2. The appropriate AC and DC voltage profiles have been generated using a Tektronix 3051 C function generator, which were amplified to the desired voltage level using a Trek 30/20 A high voltage amplifier. As shown in Figure 2b, a needle-plate design with a gap of 3 mm was employed between the needle electrode and the GFRP sample to generate corona discharges. A needle electrode with a 50- μm tip and a 6-cm diameter ground plate electrode was used in the corona inception studies. In the test cell, GFRP epoxy nanocomposite was placed between the IEC (B) electrode and the lower ground plate to create surface discharge (Figure 2c). The experimental setup also consists mainly of fluorescent fiber, DC power source, optical detector, and a DSO (a). The Type B-3(200) fluorescent fiber was acquired from Kuraray, Japan, and has an absorption and emission spectra peak at 351 and 450 nm, respectively. A SensL MicroFC SMA 10050 silicon photomultiplier (SiPM) with an excellent spectrum response (300 to 950 nm) was used in this study. A 30 V DC bias voltage was used to ensure that the photo detector worked properly. The photodetector signals were acquired using a Lecroy Model Wavepro, 7 Zi digital storage oscilloscope with a bandwidth of 3.5 GHz. For PD detection, a fiber with a length of 1 m was used in this study. In addition, a broadband UHF sensor was employed in this study to detect PD signals and a high bandwidth DSO was used to gather

the UHF signals. The UHF sensor used in the present study was pre-calibrated and used for the PD measurement. The relationship between the PD apparent discharge quantity (pC) and UHF method in reference to electromagnetic wave energy (mV) under various GIS defects is presented by Tang Ju et al. in [29]. They have indicated that the typical calibration constant as 11.6 pC/mV for field GIS calibration with a minimum sensitivity of 3 pC, with reference to the method discussed by the CIGRE A2.27 working group for GIS UHF method discharge calibration [30].

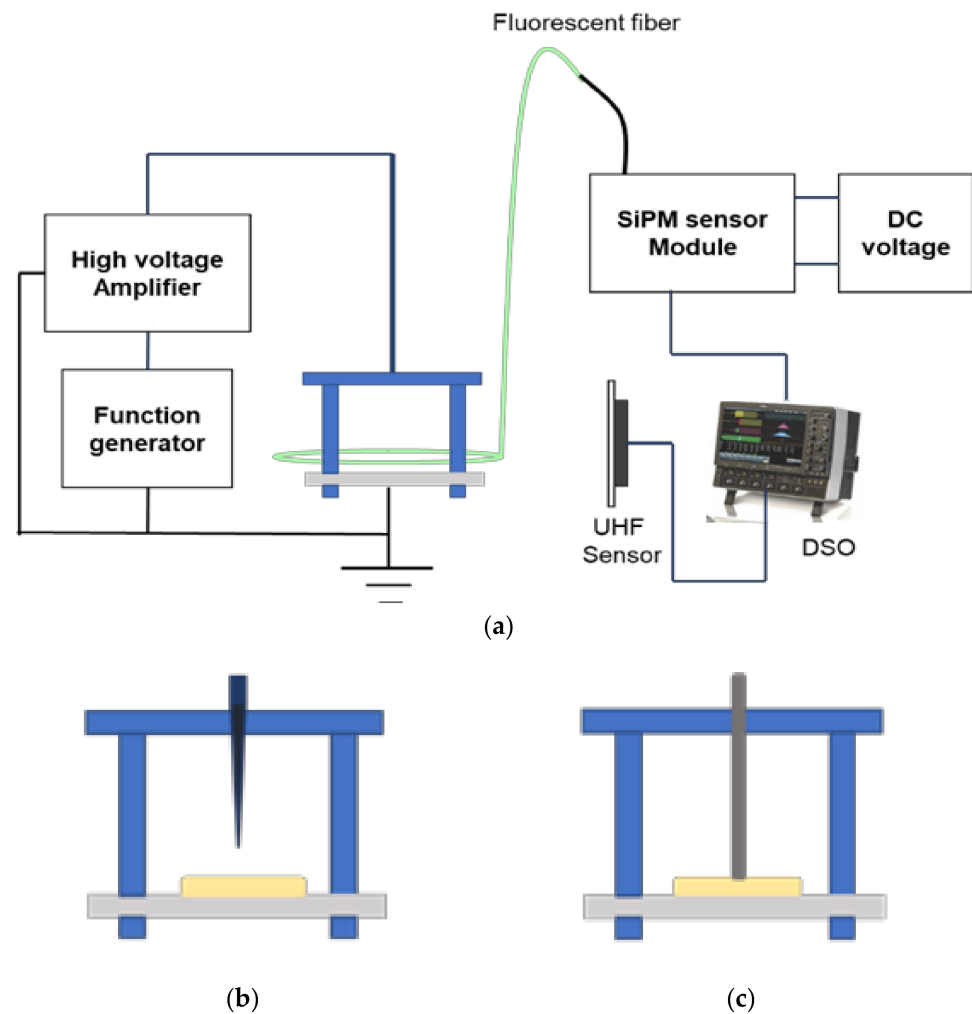


Figure 2. (a) Measurement setup of (b) corona and (c) surface discharge studies.

2.3. Surface Potential Measurement under SI Voltages

A needle-plane electrode system with positive and negative switching impulse voltages (250/2500 s) was utilized to spray charges on test materials (Figure 3). To apply high voltage, a Trek 20/20 C high voltage amplifier is used. Charges have been deposited on the sample surface at location 1, and the potential developed on the specimen surface is recorded with a Trek model 341 B electrostatic voltmeter at location 2. The test samples have dimensions of $40 \times 40 \times 0.5 \text{ mm}^3$.

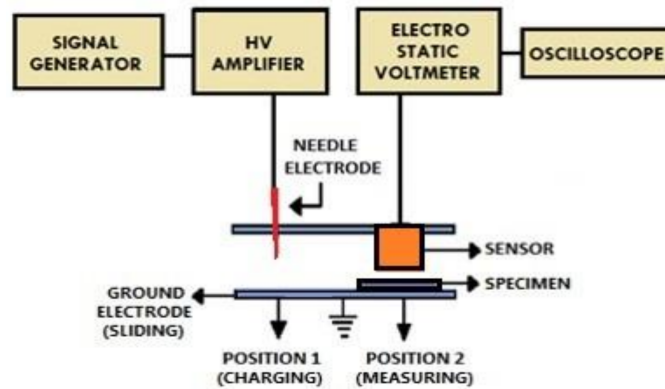


Figure 3. Setup for measuring the surface potential decay.

2.4. Space Charge Measurement

Pulse electro acoustic (PEA) method is a promising approach for detecting space charge [31]. Figure 4 shows the measurement setup for detecting space charge using the PEA technique. The basic components of the experimental setup are a Techimp PEA Flat cell and a voltage pulse generator. It also includes a Tektronix DPO5034, 350 MHz, 5 GS/s DSO, an 18–24 V DC source, and high voltage DC source (0–30 kV). The measurements of the test samples are $40 \times 40 \times 0.5 \text{ mm}^3$. As shown in Figure 5, +15 kV/mm electric field was applied across the material for 1800 s and -15 kV/mm was applied for the next 1800 s in the current experimental study. The space charge density as well as the electric field characteristics were analyzed in the present study, before and after the polarity reversal.

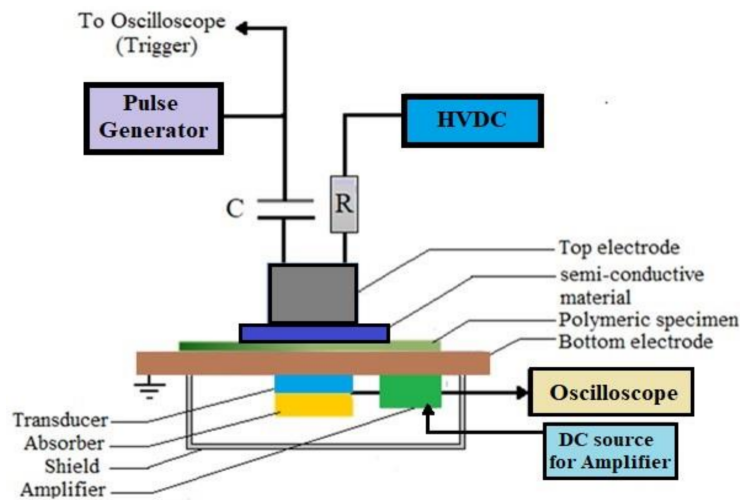


Figure 4. Space charge measurement using the PEA technique.

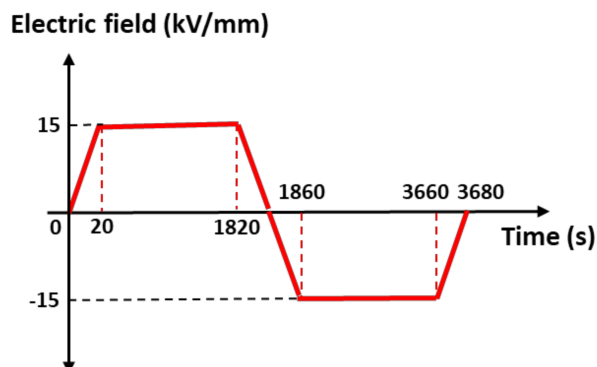


Figure 5. Timing diagram representing the polarity reversal phenomenon.

2.5. Thermal Expansion Coefficient

The coefficient of thermal expansion (CTE) is considered to be a vital thermal property of a polymer, especially in the engineering applications. Dilatometer is a thermo-analytical instrument that can measure the thermal expansion or contract of a given specimen under controlled temperature–time program. A Push-Rod Dilatometer from VB Ceramic Consultants, India, was used to investigate the coefficient of thermal expansion of GFRP nanocomposites. The sample temperature was increased from room temperature up to 60 °C using a silicon carbide heating element at the rate of 3 °C/min and the corresponding expansion in the sample is determined with a linear variable differential transformer (LVDT). The expansion that is measured digitally using the present experimental setup has a resolution of 1 µm. A sample size of 40 × 10 × 1.5 mm³, was used in the thermal expansion studies.

2.6. Thermo-Gravimetric Analysis (TGA)

Thermogravimetric analysis (TGA) is a useful tool for determining the pattern of thermal decomposition and the thermal stability of polymer composite materials. TGA studies were carried out using the SDT Q600 instrument in the temperature range of 50–750 °C under nitrogen ambience at 10 °C/min rate of heating. In the present study, the percentage weight (%) and the derivative weight (%/°C) characteristics were determined with respect to temperature. The rate of nitrogen gas was fixed at 100 mL/min. The weight of each sample used, was 5 mg. The alumina crucible was used in the present study.

3. Results and Discussion

3.1. Surface Discharge and Corona Inception Studies

Figures 6 and 7 indicate the typical fluorescence and UHF signals, along with their corresponding FFT signals generated at the point of inception of corona as well as surface discharge, respectively. The FFT analysis has been performed to the signals obtained during inception of corona activity as well as surface discharge process, to determine the range of frequencies and the dominant frequency of the UHF and fluorescence signals. The spectrum spans in the range of 0.8 to 20 MHz, having a centre frequency at 1 MHz for the fluorescence fiber. In the case of the UHF sensor, the bandwidth of the signal generated due to corona discharge and surface discharge activity lies in the range of 300 MHz to 3 GHz, having a dominant frequency near 1 GHz. It is essential to understand the correlation between the discharge magnitude in pC (adopting IEC 60270 standards) and the magnitude of UHF/Fluorescent signal formed during discharge process, which has been planned as a part of future study.

The corona discharge and surface discharge studies were repeated 10 times and a variance of less than 1% was observed. Figure 8 illustrates the variations in CIV values recorded with UHF sensor and fluorescent fiber under AC and DC voltage profiles. In comparison with UHF sensor, sensitivity in detecting the corona discharges with the fluorescent fiber is high. This might be owing to the faint and sluggish discharge current signal, which is difficult to detect with a UHF sensor than the optical signal at discharge beginning. Han et al. employed both the UHF sensor and fluorescent fiber to detect PD and found that, fluorescent fiber detects at a lower inception voltage than that of the UHF sensor [32]. Higher inception voltages were observed for the DC voltages when compared with the AC voltage. Because of zero crossing under AC voltage, the charge build-up in one half cycle was swept in the following half-cycle, lowering the net charge deposited on the sample. However, due to the local electric field opposition caused by the accumulated charge, a higher DC voltage is necessary for the discharge initiation. An increase in the inception voltage is observed with increment in the filler wt.%, up to 3 wt.%. However, further increments in nanofiller content have reduced the CIV due to the agglomerations of the nanoparticles.

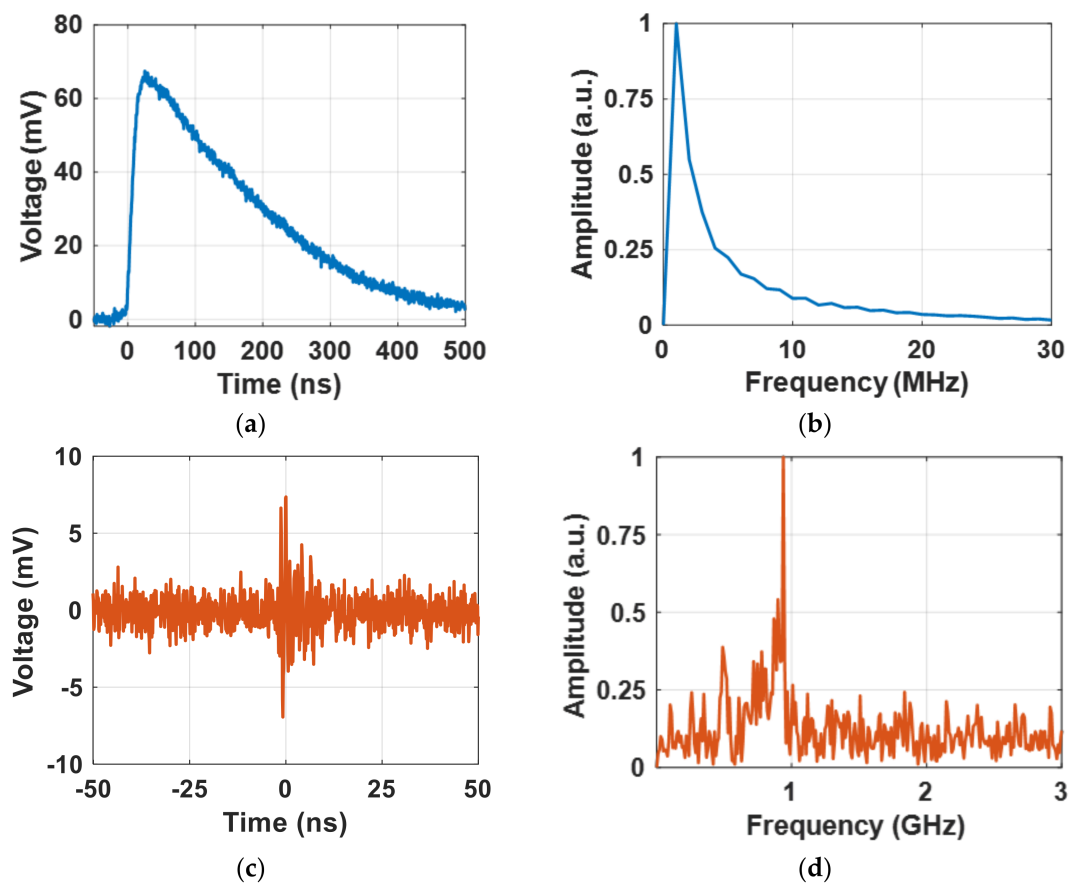


Figure 6. Typical (a) fluorescent signal, (b) FFT of fluorescent signal, (c) UHF signal, and (d) FFT of UHF signal under corona discharge studies.

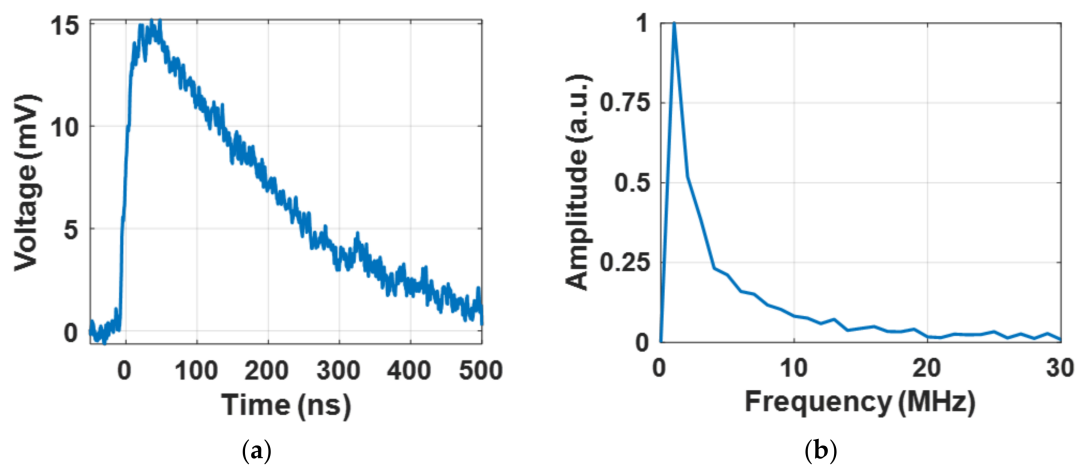


Figure 7. Cont.

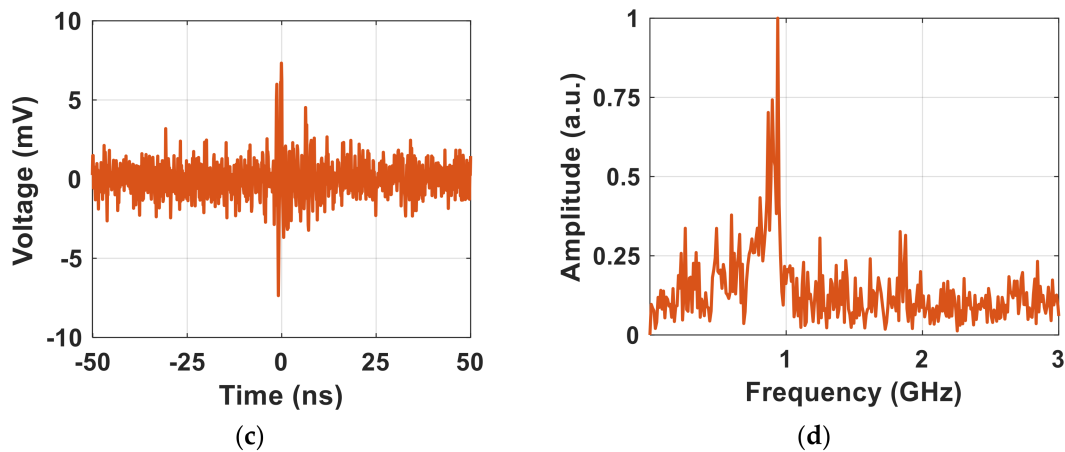


Figure 7. Typical (a) fluorescent signal, (b) FFT of fluorescent signal, (c) UHF signal, and (d) FFT of UHF signal under surface discharge studies.

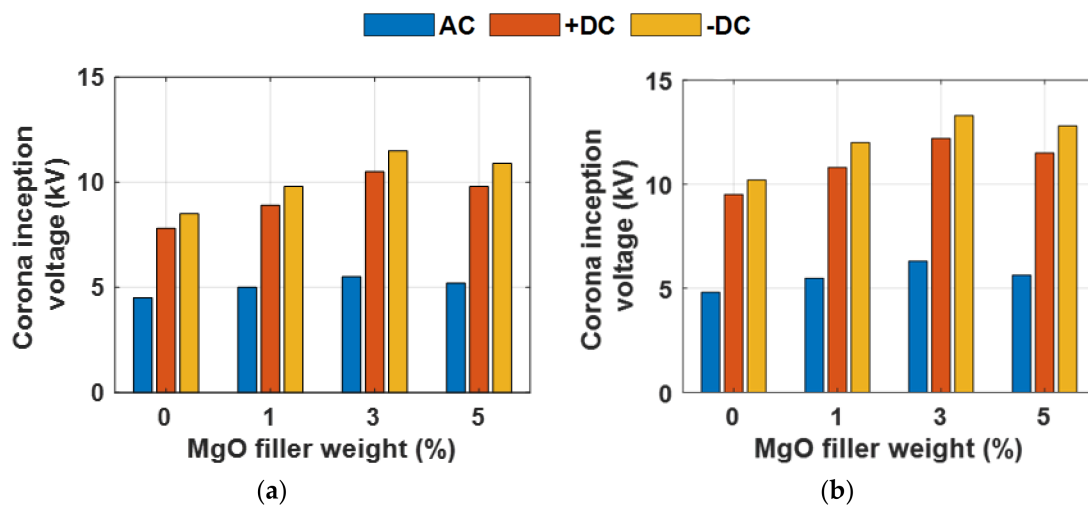


Figure 8. Variation in the CIV values detected using (a) fluorescent fiber and (b) UHF sensor.

The variations in the surface discharge inception voltage (SDIV) by keeping GFRP nanocomposite material as a barrier in the air medium using the UHF and fluorescent fiber sensor is shown in Figure 9. With steady increase in voltage, the tangential electric field at the junction of electrode, air medium, and GFRP composite material strengthens, resulting in the initiation of the surface discharge. Mu et al. performed the surface discharge measurements on different polymer materials and concluded that electric field distribution on the surface gets altered due to the change in the permittivity and the thickness of the material [33]. Kozako et al. have indicated that the improvement of partial discharge resistance of the epoxy nanocomposites upon addition of nanofillers is related to four mechanisms such as bonding strength between fillers and matrices, inter-filler space or matrix volume surrounded by neighboring fillers, morphology in the inter-filler space, and the mesoscopic interaction [34]. Because of the four mechanisms mentioned above, the surface discharge inception voltage is increased with the filler weight percentage up to 3 wt.%. Kozako et al. have also stated that the chemical bonds between nanofillers and the epoxy resins are the possible reason of their high resistance towards PD [35]. The improvement in the surface flashover voltage after nanofiller inclusion can also be attributed to the introduction of deeper traps capturing the charges [36,37]. With further increment in the filler weight percentage, reduction in the inception voltage is noticed in the case of both CIV and SDIV. It is because of the formation of agglomerations of the nanoparticles at higher filler concentrations. Distances between adjacent nanoparticles

decrease as the nanoparticle content increases, resulting in overlapped interaction zones of quasi-conductive nanoparticles that tend to increase the energy level of traps. Then the deep traps will be replaced by shallow traps leading to charge dissipation. As a result, the mobility of carriers enhances, as does the conductivity of nanocomposites. Thus, the charge carriers tend to move more easily via connected interaction zones, increasing the chances of a surface flashover [19,38]. Also, the SDIV values are lesser for AC in comparison with +DC and –DC voltages.

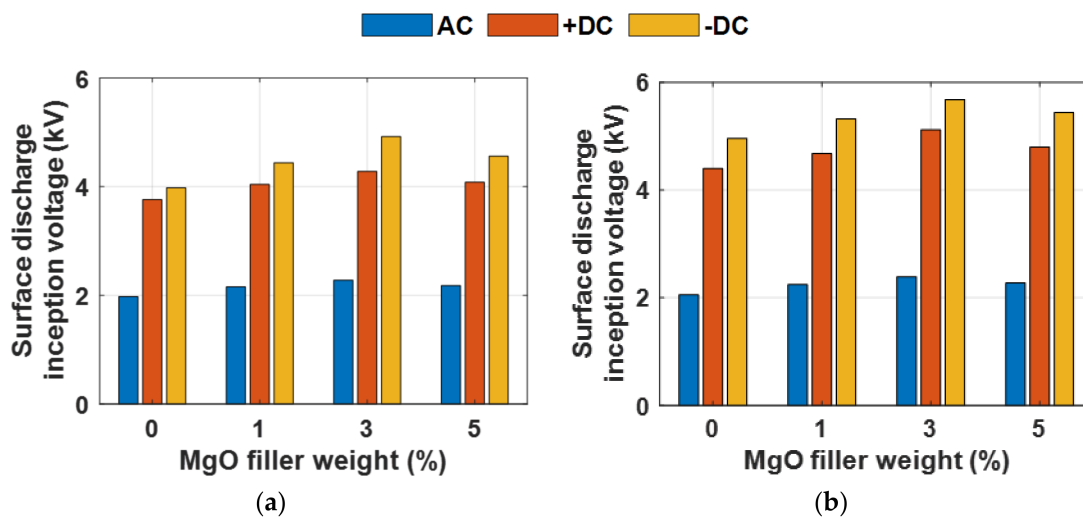


Figure 9. Variation in the SDIV values detected using (a) fluorescent fiber and (b) UHF sensor.

3.2. Surface Potential and Trap Characteristics under Switching Impulse (SI) Voltages

The surface potential characteristics obtained due to charge deposition on the surface of insulating materials (Figure 10), were modelled using exponential function as shown in (1).

$$V(t) = V_0 e^{-\lambda t} \quad (1)$$

where V_0 represents the initial surface potential and λ represents the decay rate of surface potential

The V_0 and λ of test samples are shown in Table 1. With an increase in MgO filler content up to 3 wt.%, V_0 has decreased slightly and λ of nanocomposite samples tend to increase substantially. The higher λ of the 3 wt.% sample compared to remaining test samples indicates that nanocomposite specimens accumulate less surface charge than other specimens. The decay rate of surface potential in test specimens under switching impulse voltages follows the same trend as the surface potential decay rate under positive and negative DC voltages [28]. The charge transport behavior in the material is highly influenced by the charge carrier trap states in the specimen, as well as structural impurities and aging effects. In order to fully understand the behavior of injected charge carriers trapped in localized states, the trap energy, or the energy required for the trapped carrier to escape from that localized surface state, must be calculated. The trap density function ($N(E)$) and the trap depth (ΔE) are represented as [39]:

$$N(E) = \frac{4 \epsilon_0 \epsilon_r}{q L^2 k T} t \frac{dV}{dt} \quad (2)$$

where q indicates the electron charge, L represents the thickness of the sample, k is the Boltzmann constant, t is time, and T is the absolute temperature.

$$\Delta E = E_C - E_M = kT \ln(vt) \quad (3)$$

where E_M is demarcation energy, ΔE is trap depth, E_C is conduction band energy, and ν is the attempt to escape frequency (10^{12} Hz).

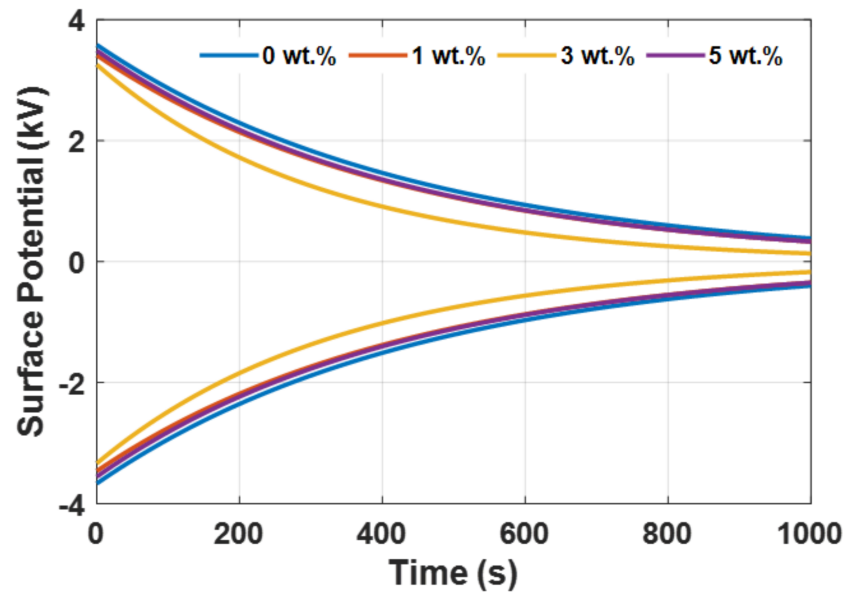


Figure 10. Surface potential decay profiles of GFRP samples.

Table 1. Surface potential, decay parameters of test samples under +SI and −SI voltage profiles.

| Sample | Positive SI | | | Negative SI | | |
|--------|-------------------------------|-------------------------|-----------------|-------------------------------|-------------------------|-----------------|
| | Initial Surface Potential (V) | Decay Rate (s^{-1}) | Trap Depth (eV) | Initial Surface Potential (V) | Decay Rate (s^{-1}) | Trap Depth (eV) |
| 0 wt.% | 3586 | 0.002235 | 0.8718 | 3669 | 0.002230 | 0.8719 |
| 1 wt.% | 3413 | 0.002332 | 0.8707 | 3463 | 0.002306 | 0.8710 |
| 3 wt.% | 3259 | 0.003188 | 0.8626 | 3337 | 0.002969 | 0.8644 |
| 5 wt.% | 3490 | 0.002356 | 0.8704 | 3557 | 0.002372 | 0.8707 |

Figure 11 shows the trap density vs. trap depth profiles of the samples. Surface charge movement on the sample surface follows three paths: towards the environment, across the surface via hopping transfer, and into the bulk of the sample. Surface trap formation is caused by physical and chemical defects like unsaturated bonds, chain ends, and molecular adsorptions. The surface charges in general are trapped by these surface traps. Through the hopping process, these trapped surface charges hop from one trap to the next, resulting in reduced charge mobility [40]. As a result, as the trap depth increases, the charge mobility decreases. The trap depth of the test samples at maximal trap density is shown in Table 1. The trap density curves shifted left when the MgO filler was added, showing a decrease in trap depth. This demonstrates that the charges in GFRP nanocomposites are trapped in shallower traps than in pure epoxy reinforced with glass fiber. This increases carrier mobility, lowering the probability of increased surface charge development. The 3 wt.% specimen had a lower trap depth, which corresponds to the highest value of trap density, showing that it outperformed other test specimens in surface potential analysis.

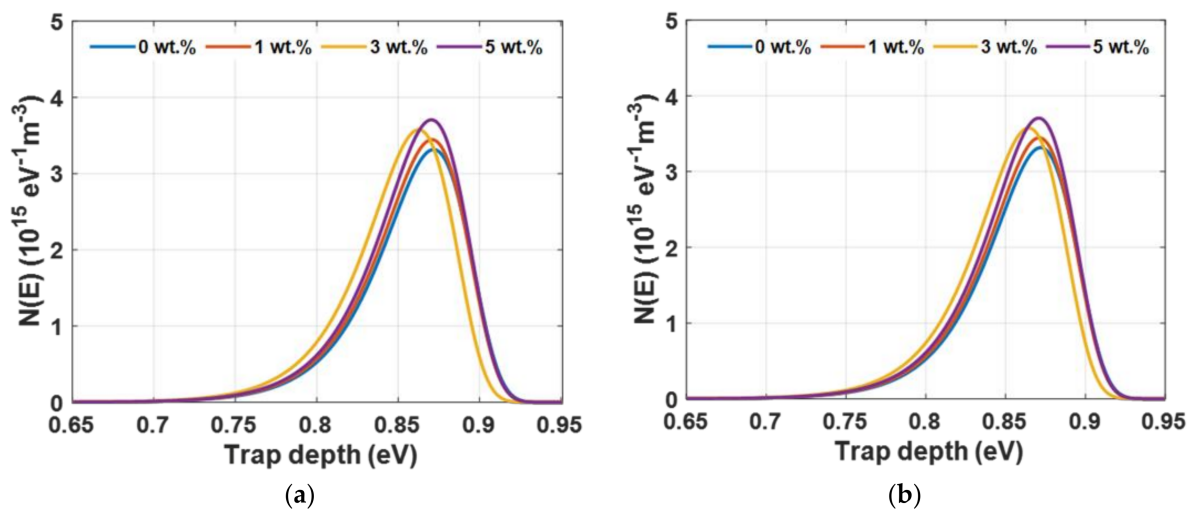


Figure 11. Trap density versus trap depth curves of test samples under (a) positive SI voltage and (b) negative SI voltage.

3.3. Space Charge Analysis during Polarity Reversal

The test samples are stressed with 15 kV/mm +DC electric field for an 1800 s poling period before the voltage polarity reversal to study the impact of polarity reversal. The voltage polarity reversal period is kept at 40 s. Post reversal, the samples are subject to a –DC stress of 15 kV/mm for 1800 s. During the polarity reversal phenomena, the variations in space charge density as well as electric field profiles of GFRP–MgO nanocomposites are depicted in Figures 12 and 13. All of the test samples show the development of hetero-charges. Heterocharges accumulated before polarity reversal will persist even after reversal, resulting in increment of the electric field near the electrode-specimen interface [41]. Figure 14 shows the space charge build-up as a function of time during the poling and depoling periods. When comparing 0 wt.% samples to nanocomposite samples, the hetero-charge formation is substantially larger for 0 wt.% materials. The addition of nanofiller creates a large number of shallow traps in the base epoxy, which improves charge carrier mobility. Thus, the space charge decay will be rapid, resulting in reduced space charge retention following polarity reversal in epoxy nanocomposites [25]. Also, MgO nanoparticles have a lower bandgap (7.8 eV) than pure epoxy (>8 eV), therefore they operate as recombination sites for free electrons and holes, substantially decreasing space charge density [17]. As a result of the lesser space charge presence during polarity reversal, the electric field enhancement is reduced. The field enhancement factor is determined as [42]:

$$F = \frac{E - E_a}{E_a} \times 100 \quad (4)$$

where, E_a indicates applied electric field stress (kV/mm), E refers to maximum electric field in the bulk of the sample (kV/mm), and F is field enhancement factor (%).

In Figure 15, the field enhancement factor of test specimens is displayed just before polarity reversal (at 1820 s), just after polarity reversal (1860 s), and after poling period of 1800 s from the reversal (at 3660 s). The field enhancement has been found to be decreasing after the MgO nanofillers have been incorporated into epoxy. In comparison to the pure epoxy sample reinforced with glass fiber, the addition of MgO nanoparticles to the epoxy resin inhibited the accumulation of space charge, resulting in lesser intensification in electric field in epoxy–MgO nanocomposites after polarity reversal (Figure 13). In comparison with other samples, the 3 wt.% sample has reflected lesser F value before and after voltage polarity reversal phenomenon.

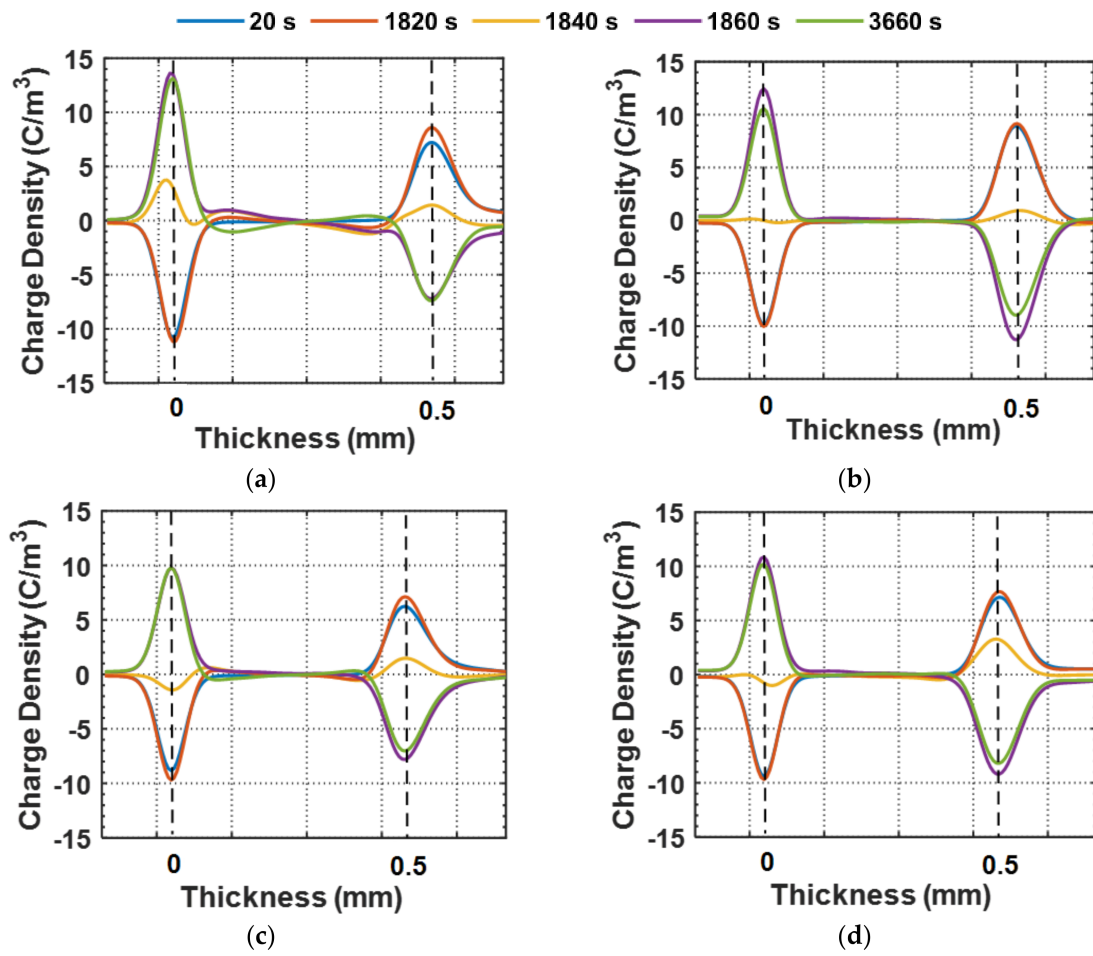


Figure 12. Space charge curves during the polarity reversal phenomenon in: (a) 0 wt.% specimen; (b) 1 wt.% specimen; (c) 3 wt.% specimen; and (d) 5 wt.% specimen.

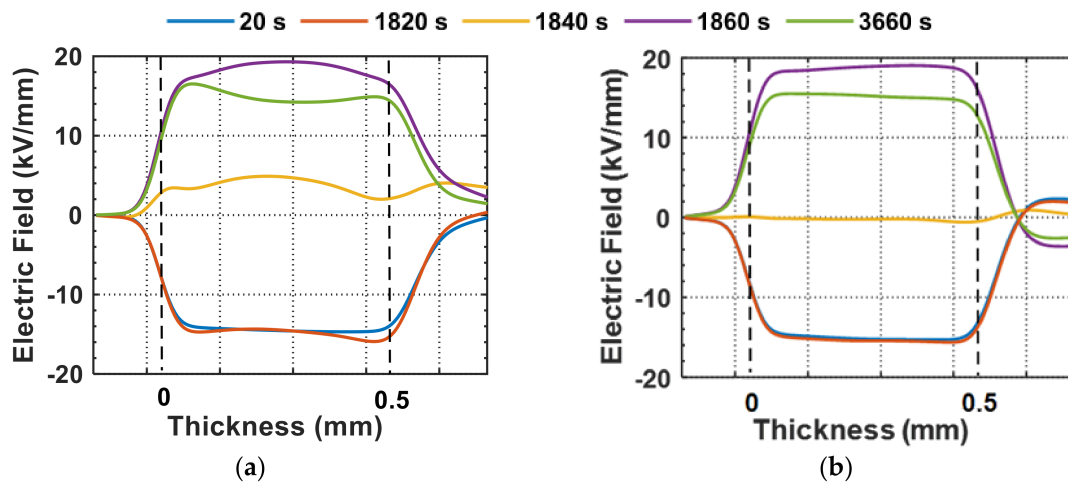


Figure 13. Cont.

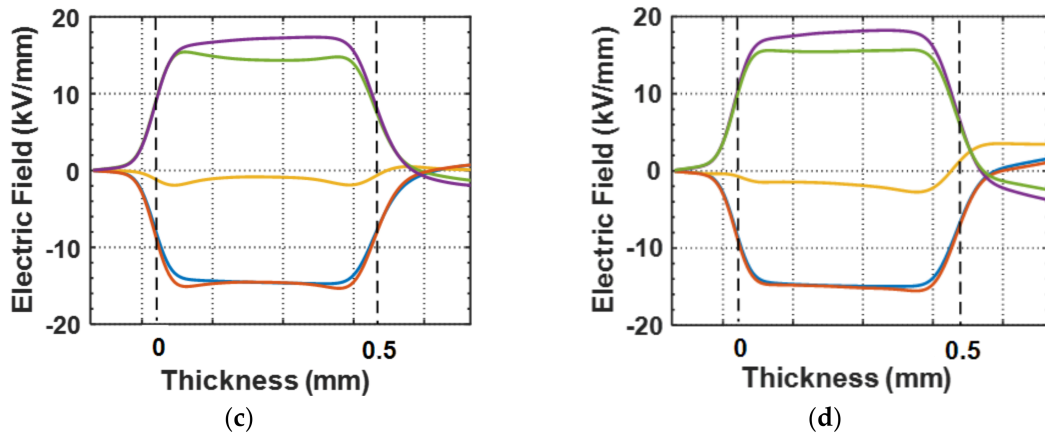


Figure 13. Electric field curves during the polarity reversal phenomenon in: (a) 0 wt.% specimen; (b) 1 wt.% specimen; (c) 3 wt.% specimen; and (d) 5 wt.% specimen.

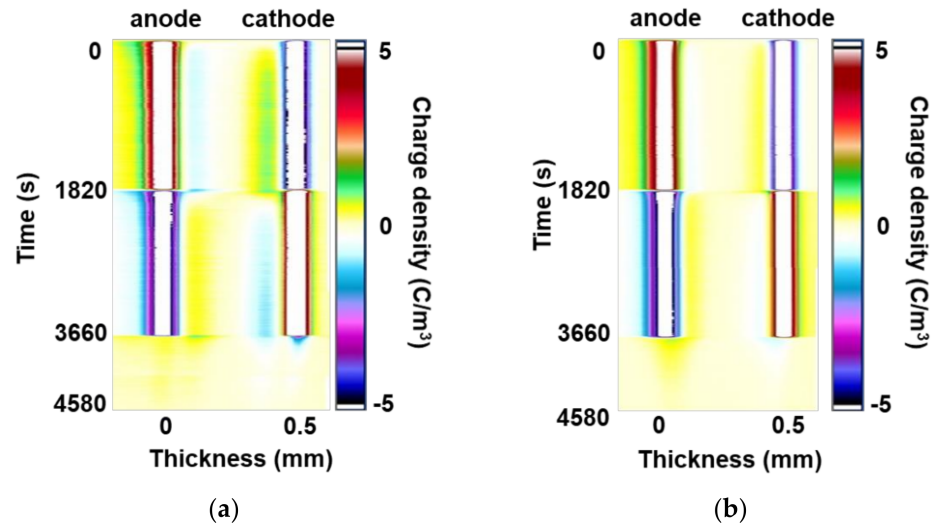


Figure 14. Space charge accumulation during the poling and depoling periods in: (a) 0 wt.% specimen and (b) 3 wt.% specimen.

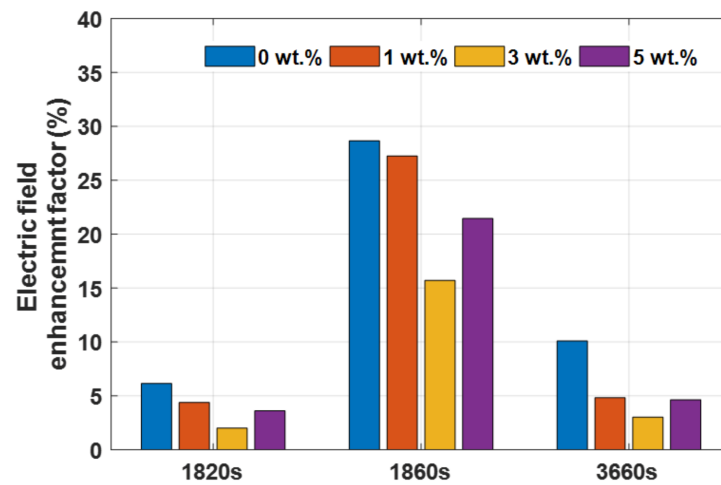


Figure 15. Timing diagram during polarity reversal phenomenon.

3.4. Coefficient of Thermal Expansion (CTE)

Introduction of stiff and low CTE filler material in to the polymer matrix can help to develop a composite material with low thermal expansion coefficient, which is generally desirable for dimensional stability. Nano MgO fillers were added to the epoxy matrix in the present study for limiting the CTE of the resulting GFRP composites. The thermal expansion coefficient is determined using the equation shown in (5) and is commonly represented as α .

$$\alpha = \frac{\Delta L}{L \Delta T} \quad (5)$$

where, L is the initial length of the specimen (mm), ΔT is the change in temperature ($^{\circ}\text{C}$), and ΔL is the change in the length of the specimen (mm).

The CTE of the different wt.% MgO nanofilled GFRP composite is depicted in Figure 16. The CTE of the composites tend to increase up to 3 wt.% as filler weight percentage increases. This is owing to the uniform dispersion of MgO nanofillers and their stiffness, which limits the movement of the epoxy matrix chains as the temperature rises. As a result, the CTE increased as the filler material has increased [43]. At higher concentrations, due to the formation of agglomerations, it becomes difficult to obstruct the epoxy chain expansions with increase in temperature and thus resulting in the increase of the CTE [43].

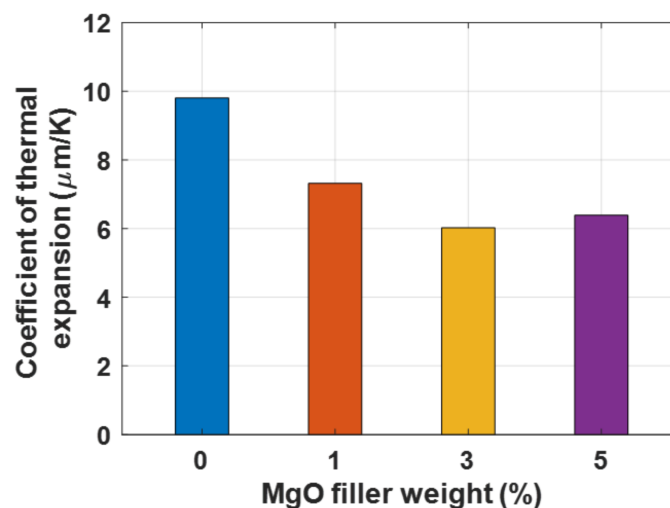


Figure 16. Thermal characteristic variation in epoxy nanocomposites.

3.5. Thermo-Gravimetric Studies

The TG and DTG characteristic curves of test specimens in the range of 50 to 750 $^{\circ}\text{C}$ are shown in Figure 17. In the current study, the weight loss of all the GFRP composite samples have occurred as a two-stage process. A small dent (a minor weight reduction peak in DTG graphs) can be seen in all specimens from 80 to 180 $^{\circ}\text{C}$ based on TG curves. This minor weight loss is produced by the vitrification effect, which causes certain polymer chains in the epoxy network to form dangling structures after curing, which are simpler to breakdown from the network even at lower decomposition temperatures. [10]. Then, it is found that all specimens are stable up to 300 $^{\circ}\text{C}$, with no additional notable weight loss. From 300 to 450 $^{\circ}\text{C}$, the TG curves indicated that the percentage weight of all test specimens decreases drastically (Figure 17).

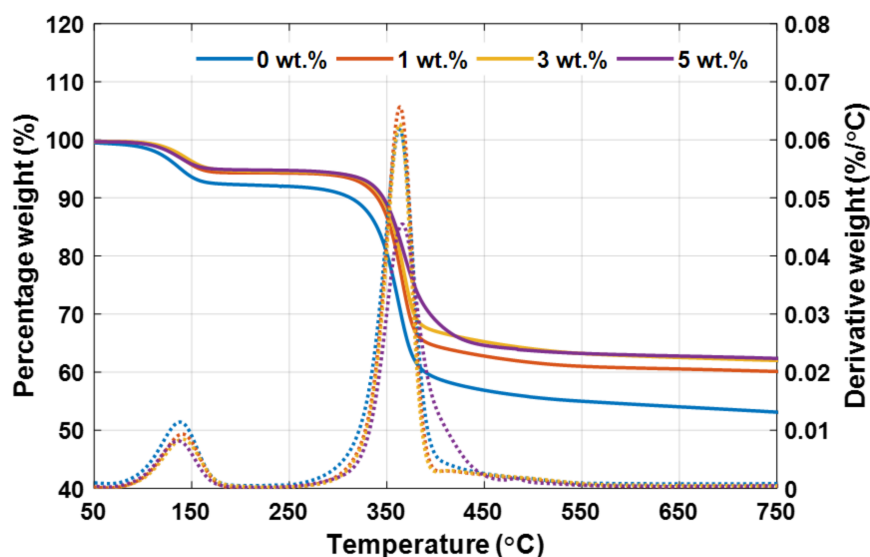


Figure 17. Thermal characteristic variation of nano-MgO filled GFRP nanocomposites.

The temperature at which maximum degradation occurred (T_{max}) and the residual weight at 750 °C are calculated from DTG and TG curves, respectively, and are presented in Table 2. T_{max} values of GFRP nanocomposites tend to increase as the MgO filler concentration increases in this study. The residual weight is one of the indicators used in the evaluation of thermal stability. When comparing pure epoxy reinforced with glass fiber to MgO nanofiller included epoxy glass fiber composites, the residual weight at 750 °C is greater. This indicates that the test samples are getting more thermally stable as MgO fillers are added. When compared to a 0 wt.% specimen, the residual weight increases dramatically with the addition of nanoparticles, up to a 3 wt.% specimen, and then only marginally increases from a 3 wt.% to a 5 wt.% specimen. Thus, it can be understood that the thermal performance of the glass fiber reinforced epoxy specimens have been improved by the addition of MgO nanofillers.

Table 2. Thermal stability parameters of nano-MgO filled GFRP nanocomposites.

| Sample | T_{max} (°C) | Residual Weight at 750 °C (%) |
|--------|----------------|-------------------------------|
| 0 wt.% | 362.6 | 52.70 |
| 1 wt.% | 363.1 | 59.87 |
| 3 wt.% | 363.4 | 61.76 |
| 5 wt.% | 365.4 | 62.05 |

4. Conclusions

The following important conclusions have been accrued from the current research work.

- Increments in MgO filler weight percentage up to 3 wt.% tend to enhance surface discharge and corona inception voltages measured using fluorescence and UHF methods, under both AC and DC voltage profiles.
- Reduced initial surface potential and increased λ is noticed after inclusion of MgO nanoparticles. In comparison to other test samples, the 3 wt.% specimen shows higher λ value and lower trap depth at peak trap density, reflecting the presence of relatively shallower traps.
- Before and after the polarity reversal phenomena, heterocharge formation is seen in the bulk of test specimens. In comparison with other test samples, the 3 wt.% specimen had a lower electric field enhancement factor.
- After MgO filler was added to GFRP nanocomposites, the CTE values have reduced, with the 3 wt.% specimen having the lowest CTE value.

- TGA measurements revealed an increase in Tmax and residual weight in nano MgO filled GFRP composites, showing that the thermal stability of the GFRP composites has increased after incorporation of MgO nanoparticles.

Overall, the GFRP nanocomposite sample filled with 3 wt.% nano-MgO outperformed the other test specimens in terms of electrical and thermal performance.

Author Contributions: All the authors have contributed equally in the present research work. All authors have read and agreed to the published version of the manuscript.

Funding: Author (R.S.) wishes to thank CPRI, Bangalore, India for sponsoring the project (NPP/2016/TR/1/27042016) on nanocomposites.

Institutional Review Board Statement: Not applicable.

Informed Consent Statement: Not applicable.

Data Availability Statement: The data that support the findings of this study are available from the corresponding author upon reasonable request.

Conflicts of Interest: The authors declare no conflict of interest.

References

1. Tanaka, T.; Imai, T. *Advanced Nanodielectrics: Fundamentals and Applications*, 2nd ed.; Pan Stanford Publishing: Singapore, 2017.
2. Silwal, B.; Sergeant, P. Thermally Induced Mechanical Stress in the Stator Windings of Electrical Machines. *Energies* **2018**, *11*, 2113. [[CrossRef](#)]
3. Verginadis, D.; Karlis, A.; Danikas, M.G.; Antonino-Daviu, J.A. Investigation of Factors Affecting Partial Discharges on Epoxy Resin: Simulation, Experiments, and Reference on Electrical Machines. *Energies* **2021**, *14*, 6621. [[CrossRef](#)]
4. Danikas, M.G.; Sarathi, R. Electrical machine insulation: Traditional insulating materials, nanocomposite polymers and the question of electrical trees. *Funktechnikplus# J.* **2014**, *1*, 7.
5. Danikas, M.G.; Karlis, A. Some observations on the dielectric breakdown and the importance of cavities in insulating materials used for cables and electrical machines. *Adv. Electr. Comp. Eng.* **2011**, *11*, 123–126. [[CrossRef](#)]
6. Andraschek, N.; Wanner, A.J.; Ebner, C.; Riess, G. Mica/Epoxy-Composites in the Electrical Industry: Applications, Composites for Insulation, and Investigations on Failure Mechanisms for Prospective Optimizations. *Polymers* **2016**, *8*, 201. [[CrossRef](#)]
7. Hornak, J.; Mentlík, V.; Trnka, P.; Šutta, P. Synthesis and Diagnostics of Nanostructured Micaless Microcomposite as a Prospective Insulation Material for Rotating Machines. *Appl. Sci.* **2019**, *9*, 2926. [[CrossRef](#)]
8. Muto, H. Dielectric Breakdown and Partial Discharge Properties of Nanocomposites for Epoxy/Mica Insulation system in Large-size Rotating Machines. In Proceedings of the International Symposium on Electrical Insulating Materials, Tokyo, Japan, 13–17 September 2020; p. 45.
9. Hildinger, T.; Weidner, J.R. Progress in development of a nanocomposite stator winding insulation system for improved generator performance. In Proceedings of the Electrical Insulation Conference, Baltimore, MD, USA, 11–14 June 2017; p. 139.
10. Wang, S.; Chen, Y.; Mao, J.; Liu, C.; Zhang, L.; Cheng, Y.; Du, C.; Tanaka, T. Dielectric strength of glass fibre fabric reinforced epoxy by nano-Al₂O₃. *IEEE Trans. Dielectr. Electr. Insul.* **2020**, *27*, 1086–1094. [[CrossRef](#)]
11. Abd Rahman, M.S.; Ab Kadir, M.Z.A.; Abd Rahman, M.S.; Osman, M.; Mohd Nor, S.F.; Zainuddin, N.M. Investigation of Insulation Characteristics of GFRP Crossarm Subjected to Lightning Transient. *Energies* **2021**, *14*, 4386. [[CrossRef](#)]
12. Bazli, M.; Abolfazli, M. Mechanical Properties of Fiber Reinforced Polymers under Elevated Temperatures: An Overview. *Polymers* **2020**, *12*, 2600. [[CrossRef](#)]
13. Andritsch, T.; Kochetov, R.; Morshuis, P.H.; Smit, J.J. Dielectric properties and space charge behavior of MgO-epoxy nanocomposites. In Proceedings of the International Conference on Solid Dielectrics, Potsdam, Germany, 4–9 July 2010; p. 1.
14. Wu, K.; Wang, Z.; Zhao, C.; Huang, Y.; Li, J.; Li, S. Surface treeing and segmented worm model of tracking behavior in MgO/Epoxy nanocomposites. *IEEE Trans. Dielectr. Electr. Insul.* **2018**, *25*, 2067–2075. [[CrossRef](#)]
15. Xing, Z.; Zhang, C.; Hu, X.; Guo, P.; Zhang, J.; Wang, Z.; Wu, K.; Li, J. Surface tracking of MgO/epoxy nanocomposites: Effect of surface hydrophobicity. *Appl. Sci.* **2019**, *9*, 413. [[CrossRef](#)]
16. Hornak, J.; Trnka, P.; Kadlec, P.; Michal, O.; Mentlík, V.; Šutta, P.; Csányi, G.M.; Tamas, Z.Á. Magnesium oxide nanoparticles: Dielectric properties, surface functionalization and improvement of epoxy-based composites insulating properties. *Nanomaterials* **2018**, *8*, 381. [[CrossRef](#)]
17. Andritsch, T.; Kochetov, R.; Lennon, B.; Morshuis, P.H.; Smit, J.J. Space charge behavior of magnesium oxide filled epoxy nanocomposites at different temperatures and electric field strengths. In Proceedings of the Electrical Insulation Conference, Annapolis, MD, USA, 5–8 June 2011; p. 136.
18. Nitta, T.; Chiba, M.; Uematsu, H. Characteristic of AC surface spark voltage in LN₂ and LHe. *IEEE Trans. Appl. Supercond.* **2000**, *10*, 1325–1328. [[CrossRef](#)]

19. Verginadis, D.; Danikas, M.G.; Sarathi, R. Study of the phenomena of surface discharges and flashover in nanocomposite epoxy resin under the influence of homogeneous electric fields. *Eng. Technol. Appl. Sci. Res.* **2019**, *9*, 4315–4321.
20. Sarathi, R.; Giridhar, A.V.; Sethupathi, K. Understanding the incipient discharge activity in liquid nitrogen under AC voltage by adopting UHF technique. *IEEE Trans. Dielectr. Electr. Insul.* **2011**, *18*, 707–713. [[CrossRef](#)]
21. Farenc, J.; Mangeret, R.; Boulanger, A.; Destruel, P.; Lescure, M. A fluorescent plastic optical fiber sensor for the detection of corona discharges in high voltage electrical equipment. *Rev. Sci. Instrum.* **1994**, *65*, 155–160. [[CrossRef](#)]
22. Naveen, J.; Sarathi, R.; Srinivasan, B. Fluorescent fiber-based identification of incipient discharges in liquid nitrogen. *Cryogenics* **2021**, *120*, 103376. [[CrossRef](#)]
23. Muto, K. Electric-discharge sensor utilizing fluorescent optical fiber. *J. Lightwave Technol.* **1989**, *7*, 1029–1032. [[CrossRef](#)]
24. Chen, G.; Hao, M.; Xu, Z.; Vaughan, A.; Cao, J.; Wang, H. Review of high voltage direct current cables. *CSEE J. Power Energy Syst.* **2015**, *1*, 9. [[CrossRef](#)]
25. Chen, X.; Wang, X.; Wu, K.; Peng, Z.R.; Cheng, Y.H.; Tu, D.M. Effect of voltage reversal on space charge and transient field in LDPE films under temperature gradient. *IEEE Trans. Dielectr. Electr. Insul.* **2012**, *19*, 140–149. [[CrossRef](#)]
26. Du, B.X.; Li, A. Effects of DC and pulse voltage combination on surface charge dynamic behaviors of epoxy resin. *IEEE Trans. Dielectr. Electr. Insul.* **2017**, *24*, 2025–2033. [[CrossRef](#)]
27. Seretis, G.V.; Nitodas, S.F.; Mimigianni, P.D.; Kouzilos, G.N.; Manolakos, D.E.; Provatidis, C.G. On the post-curing of graphene nanoplatelets reinforced hand lay-up glass fabric/epoxy nanocomposites. *Compos. B Eng.* **2018**, *140*, 133–138. [[CrossRef](#)]
28. Naveen, J.; Babu, M.S.; Sarathi, R. Impact of MgO nanofiller-addition on electrical and mechanical properties of glass fiber reinforced epoxy nanocomposites. *J. Polym. Res.* **2021**, *28*, 377. [[CrossRef](#)]
29. Ju, T.; Zhongrong, X.; Xiaoxing, Z.; Caixin, S. GIS partial discharge quantitative measurements using UHF microstrip antenna sensors. In Proceedings of the Conference on Electrical Insulation and Dielectric Phenomena, Vancouver, BC, Canada, 14–17 October 2007; p. 116.
30. Boeck, W.; Albiez, M.; Bengtsson, T.; Diessner, A.; Feger, R.; Feser, K.; Girodet, A.; Galski, E.; Hampton, B.F.; Hücker, T.; et al. Partial discharge detection system for GIS: Sensitivity Verification for the UHF method and the acoustic method. *ÉLECTRA* **1999**, *183*, 75–87.
31. Ahmed, N.H.; Srinivas, N.N. Review of space charge measurements in dielectrics. *IEEE Trans. Dielectr. Electr. Insul.* **1997**, *4*, 644–656. [[CrossRef](#)]
32. Han, X.; Li, J.; Zhang, L.; Pang, P.; Shen, S. A novel PD detection technique for use in GIS based on a combination of UHF and optical sensors. *IEEE Trans. Instrum. Meas.* **2018**, *68*, 2890–2897. [[CrossRef](#)]
33. Mu, H.B.; Zhang, G.J.; Komiyama, Y.; Suzuki, S.; Miyake, H.; Tanaka, Y.; Takada, T. Investigation of surface discharges on different polymeric materials under HVAC in atmospheric air. *IEEE Trans. Dielectr. Electr. Insul.* **2011**, *18*, 485–494.
34. Kozako, M.; Kido, R.; Imai, T.; Ozaki, T.; Shimizu, T.; Tanaka, T. Surface roughness change of epoxy/TiO₂ nanocomposites due to partial discharges. In Proceedings of the International Symposium on Electrical Insulating Materials, Kitakyushu, Japan, 5–9 June 2005; p. 661.
35. Kozako, M.; Fuse, N.; Ohki, Y.; Okamoto, T.; Tanaka, T. Surface degradation of polyamide nanocomposites caused by partial discharges using IEC (b) electrodes. *IEEE Trans. Dielectr. Electr. Insul.* **2004**, *11*, 833–839. [[CrossRef](#)]
36. Du, B.X.; Li, J.; Du, Q.; Fu, M.L. Surface charge and flashover voltage of EVA/CB nanocomposite under mechanical stresses. *IEEE Trans. Dielectr. Electr. Insul.* **2016**, *23*, 3734–3741. [[CrossRef](#)]
37. Yu, S.; Li, S.; Wang, S.; Huang, Y.; Tariq Nazir, M.; Phung, B.T. Surface flashover properties of epoxy based nanocomposites containing functionalized nano-TiO₂. *IEEE Trans. Dielectr. Electr. Insul.* **2018**, *25*, 1567–1576.
38. Charalambous, C.; Danikas, M.G.; Yin, Y.; Vordos, N.; Nolan, J.W.; Mitropoulos, A. Study of the behavior of water droplets under the influence of a uniform electric field on conventional polyethylene and on crosslinked polyethylene (XLPE) with MgO nanoparticles samples. *Eng. Technol. Appl. Sci. Res.* **2017**, *7*, 1323–1328. [[CrossRef](#)]
39. Simmons, J.G.; Tam, M.C. Theory of isothermal currents and the direct determination of trap parameters in semiconductors and insulators containing arbitrary trap distributions. *Phys. Rev. B* **1973**, *7*, 3706. [[CrossRef](#)]
40. Gao, Y.; Li, Z.; Wang, M.; Du, B. Magnetic field induced variation in surface charge accumulation behavior on epoxy/Al₂O₃ nanocomposites under DC stress. *IEEE Trans. Dielectr. Electr. Insul.* **2019**, *26*, 859–867. [[CrossRef](#)]
41. Fabiani, D.; Montanari, G.C.; Dardano, A.; Guastavino, G.; Testa, L.; Sangermano, M. Space charge dynamics in nanostructured epoxy resin. In Proceedings of the Annual Report Conference on Electrical Insulation and Dielectric Phenomena, Quebec, QC, Canada, 26–29 October 2008; p. 710.
42. Liu, P.; Ning, X.; Peng, Z.; Xiang, Z.; Feng, H.; Zhang, H. Effect of temperature on space charge characteristics in epoxy resin. *IEEE Trans. Dielectr. Electr. Insul.* **2015**, *22*, 65–71. [[CrossRef](#)]
43. Yasmin, A.; Daniel, I.M. Mechanical and thermal properties of graphite platelet/epoxy composites. *Polymer* **2004**, *45*, 8211–8219. [[CrossRef](#)]